Electronic Supplementary Material (ESI) for Journal of Materials Chemistry A.

Supporting Information

Insights into the exceeding capacity of interlayer-expanded MoS_2 as a Li-ion intercalation host

Shan Gong,[a] *Guangyu Zhao,*[b]* *Pengbo Lyu,*[c] *Kening Sun*[b]*

[a]School of Chemistry and Chemical Engineering, Harbin Institute of Technology, Harbin 150001, P. R. China

[b]Academy of Fundamental and Interdisciplinary Sciences, Harbin Institute of Technology, Harbin 150001, P. R. China

[c]Department of Physical and Macromolecular Chemistry, Charles University, Hlavova 2030, Prague 2, Prague 12843, Czech Republic

*E-mail: keningsunhit@126.com; zhaogy810525@gmail.com

Kinetics analysis (calculating the *b*-value and capacitive-type charge storage)

The dependency of the current response on the sweep rate in a cyclic voltammetry experiment can be utilized to distinguish the charge storage process according to Equation (1):[1,2]

$$i = av^b \qquad (1)$$

i is fit to a power law with scan rate v, and the exponential term b can be determined from the slope of the $log(i)$ versus $log(v)$ plot. Values of $b = 0.5$ indicate that the current is proportional to the square root of the scan rate, which is consistent with traditional diffusion dominated charge storage. On the other hand, when $b = 1$ the current is linearly proportional to the scan rate, which is characteristic of a capacitor-like charge storage mechanism.

At a particular potential, the current is contributed from both capacitive and diffusion behaviours, thus, the capacitive contributions can be identified by the following Equation (2):[3]

$$i = k_1 v + k_2 v^{1/2} \qquad (2)$$

$k_1 v$ and $k_2 v^{0.5}$ correspond to capacitive and diffusion contributions to the measured current, respectively, where v is the scan rate in mV s^{-1}.

Impedance Spectroscopy Analysis (calculating the Warburg coefficient (σ))

The Li-ion diffusion coefficient (D_{Li}) can be calculated based on the following Equation (3):[4]

$$D_{Li} = \frac{R^2T^2}{2A^2n^4F^4C^2\sigma^2} \qquad (3)$$

Here, R is the gas constant, T is the absolute temperature, A is the surface area of the cathode, n is the number of electrons per molecule attending the electronic transfer reaction, F is Faraday constant, C is the concentration of lithium ion, and σ is the Warburg coefficient associated with the slope of the linear fittings in the low frequency region. The value of D_{Li} has the positive

relationship with $1/\sigma^2$, so the trend of $1/\sigma^2$ reflects the changes of D_{Li}.

In addition, σ has the relationship with Z_{re} according to Equation (4):[4]

$$Z_{re} = R_s + R_f + \sigma\omega^{-0.5} \quad (4)$$

So the value of σ is the slope of the graph of Z_{re} against $\omega^{-0.5}$ in the low frequency region.

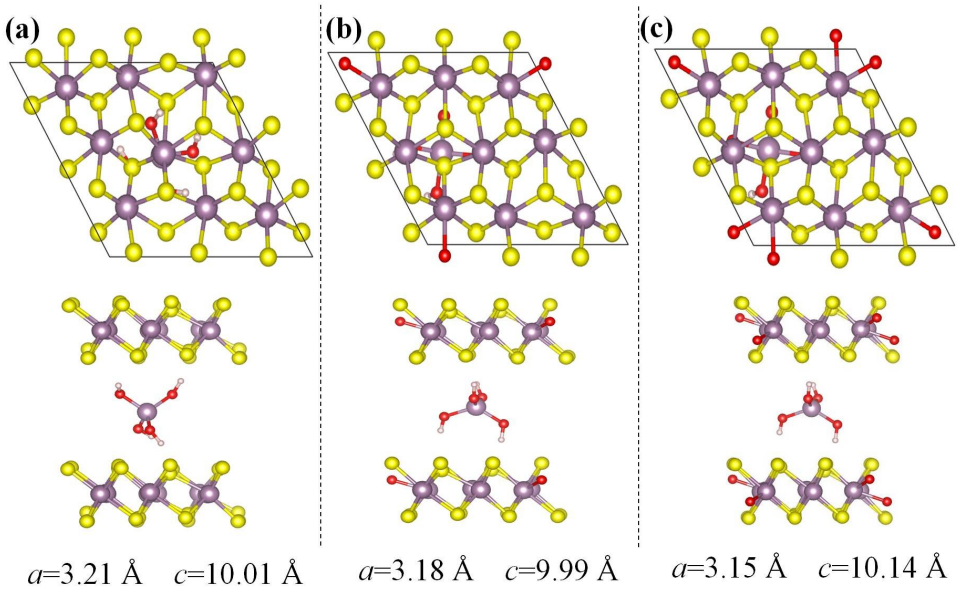

Figure S1. The atomic structures of molybdenum species ($Mo(OH)_4$) incorporated into MoS_2 with corresponding lattice constants. Three situations are considered: (a) no sulfur atom is substituted by oxygen atom; (b) one sulfur atom is substituted by oxygen atom in one unit of MoS_2; (c) two sulfur atoms are substituted by oxygen atom in one unit of MoS_2. The calculated interlayer spacing is around 10.0 Å, close to the interlayer distance of O-MoS_2 HNS in the experiment.

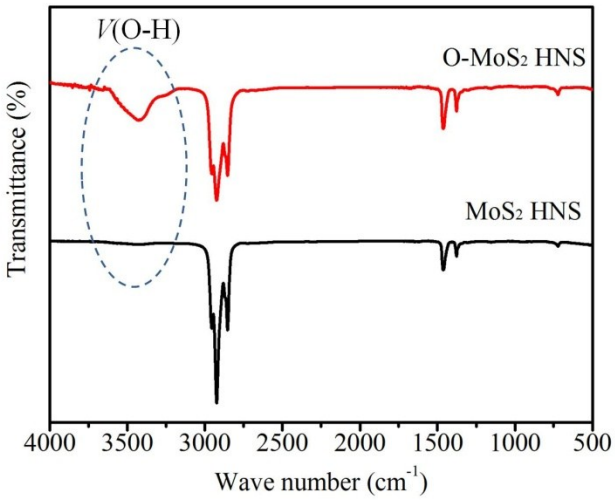

Figure S2. FT-IR spectra results of O-MoS_2 HNS and MoS_2 HNS in paraffin oil. The O–H stretch vibration of O-MoS_2 HNS is found at around 3400 cm^{-1}, while no signal from hydroxyl groups is detected in MoS_2 HNS. The hydroxyl groups in O-MoS_2 HNS should come from the incorporated $Mo(OH)_4$ species. The signals between 3000 and 500 cm^{-1} are attributed to the paraffin oil.

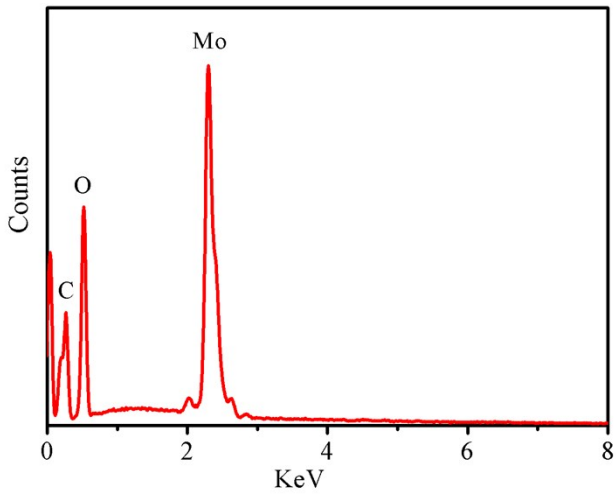

Figure S3. EDS spectrum of the MoG spheres.

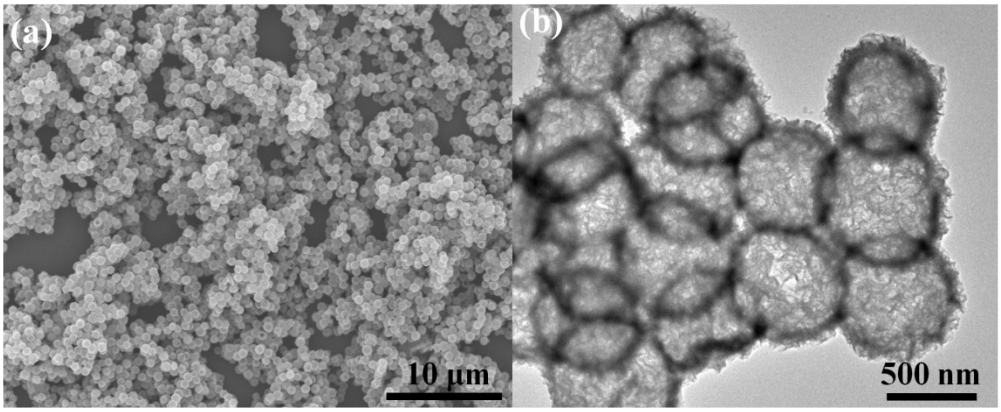

Figure S4. Low magnification (a) SEM and (b) TEM images of O-MoS_2 HNS.

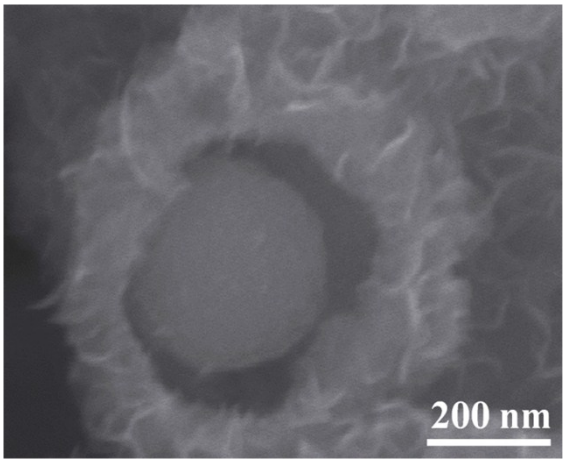

Figure S5. SEM image of the product after a shortened sulfidation process (3h).

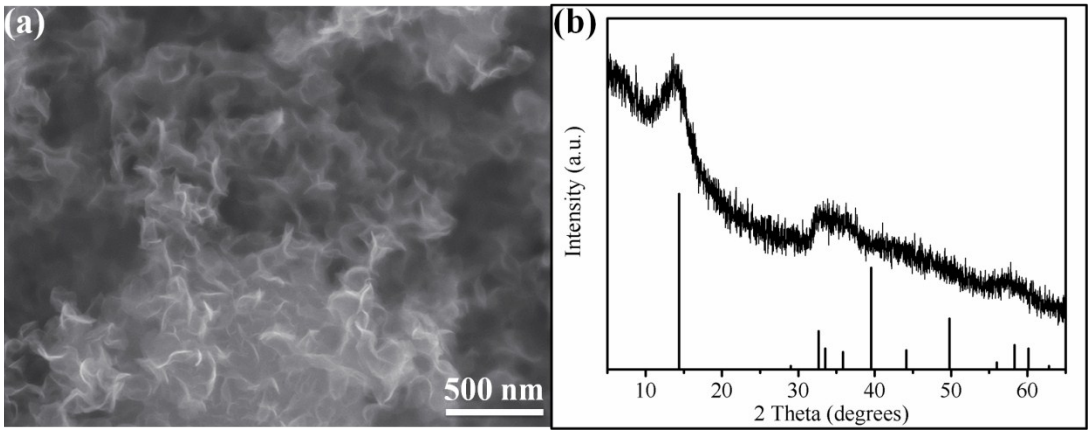

Figure S6. (a) SEM image of the MoS_2 nanosheets when the sulfidation temperature rising to 220 °C with the other conditions of the reaction are identical to that of O-MoS_2 HNS. (b) XRD pattern of as-obtained MoS_2 nanosheets. It is assigned to standard pattern of MoS_2 (JCPDS Card No. 37-1492).

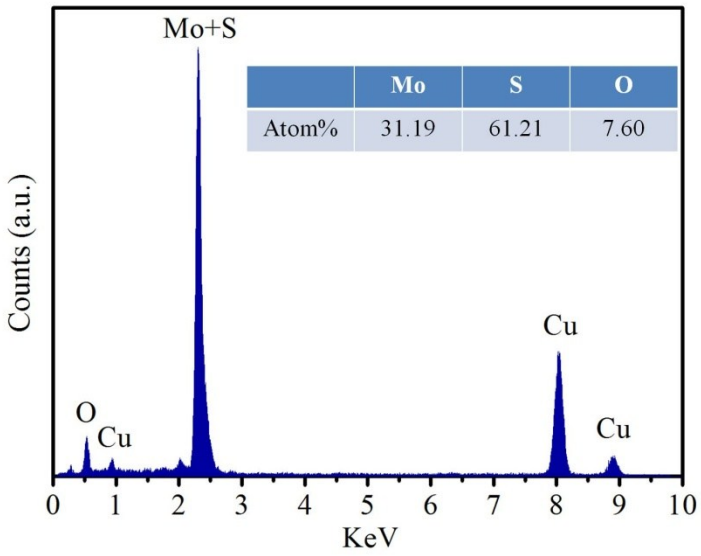

Figure S7. EDS spectrum of O-MoS_2 HNS. The inset table is the corresponding element contents.

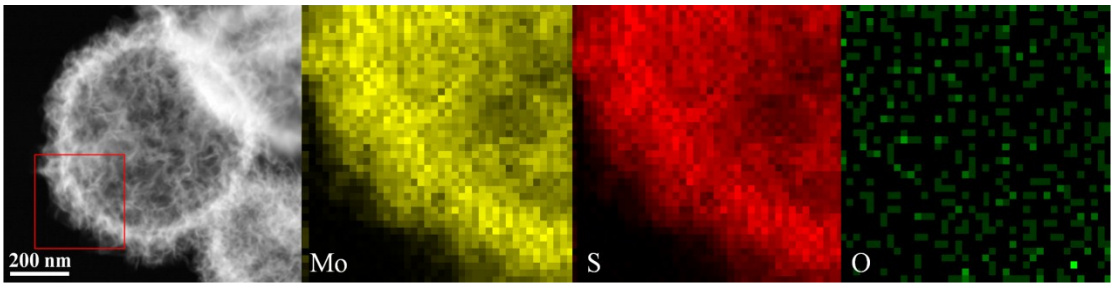

Figure S8. Element mapping images of MoS_2 HNS. Rare O element is found in MoS_2 HNS.

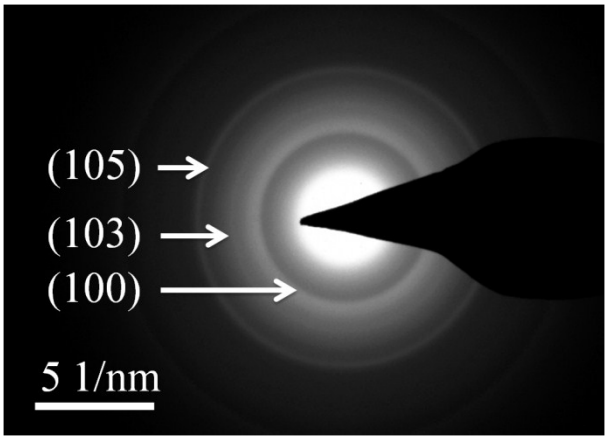

Figure S9. SAED pattern of O-MoS_2 HNS.

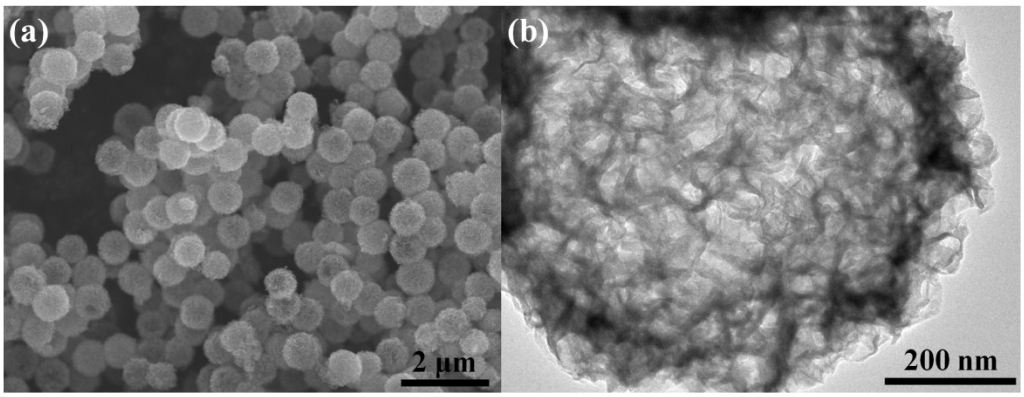

Figure S10. (a) Low magnification SEM image and (b) TEM image of MoS_2 HNS.

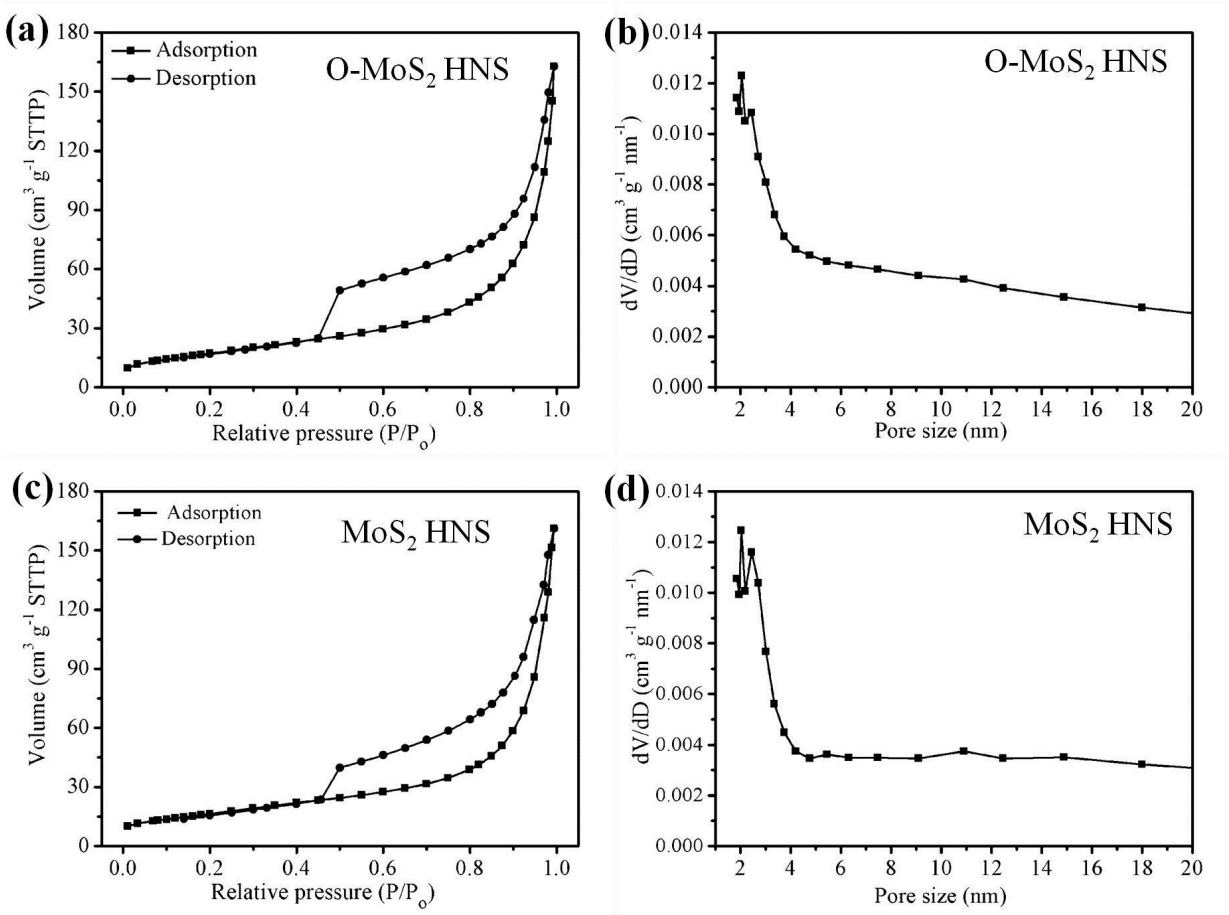

Figure S11. (a) N_2 adsorption-desorption isotherms of (a) O-MoS_2 HNS and (c) MoS_2 HNS. The BJH pore size distribution curves of (b) O-MoS_2 HNS and (d) MoS_2 HNS. The Brunauer-Emmett-Teller specific surface areas of O-MoS_2 HNS and MoS_2 HNS are 63.5 and 60.3 $m^2\ g^{-1}$, respectively.

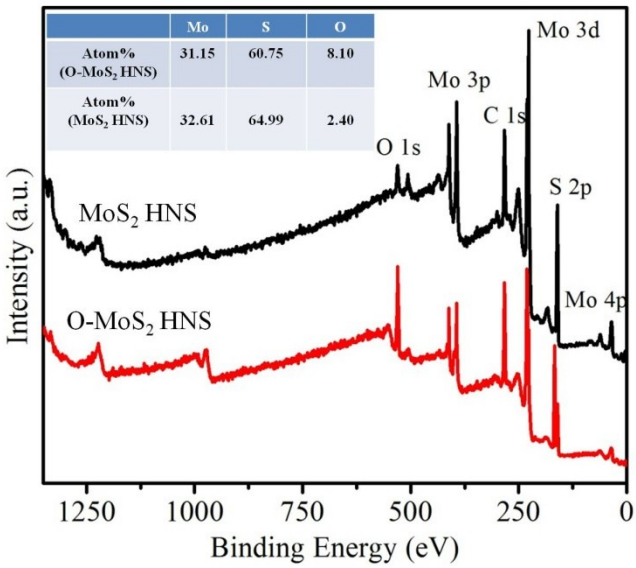

Figure S12. (a) XPS spectra of O-MoS_2 HNS and MoS_2 HNS. The inset table is the corresponding element contents.

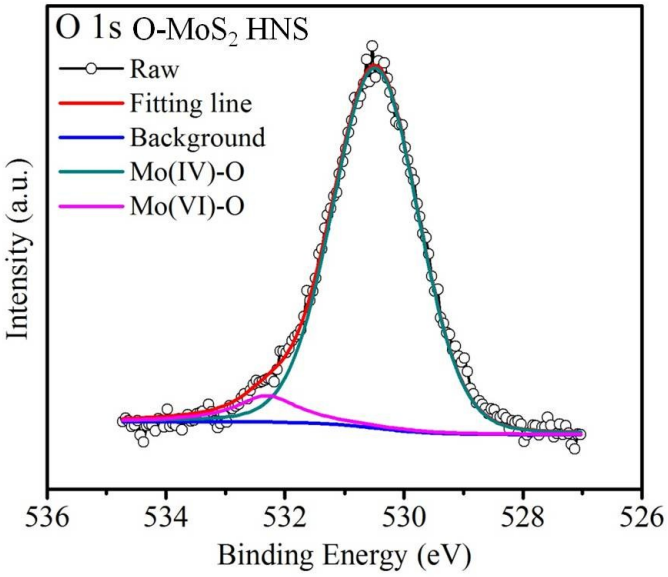

Figure S13. O 1s spectrum of O-MoS_2 HNS.

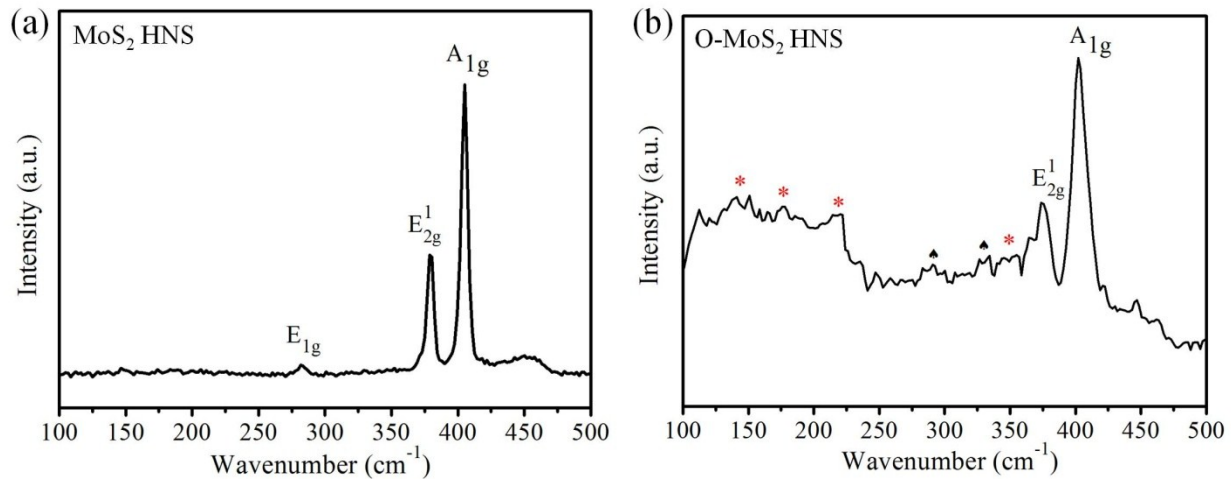

Figure S14. Raman spectra of (a) MoS_2 HNS and (b) O-MoS_2 HNS. MoS_2 HNS produces data characteristic of the 2H phase with peaks at 281, 377, and 403 cm^{-1}, which corresponds to E_{1g}, E_{2g}, and A_{1g} symmetries, respectively. The large peaks at 377 and 403 cm^{-1} are also observed in O-MoS_2 HNS, in addition, four new peaks are observed in the O-MoS_2 HNS (labeled with ∗ at around 150, 178, 222, and 346 cm^{-1}), confirming the existence of the 1T phase. The peaks at around 285 and 334 cm^{-1} (labeled with ♠) can be identified as the B_{2g} and B_{1g} vibrational modes for Mo-O bonds, thus proving the successful oxygen incorporation in the product.

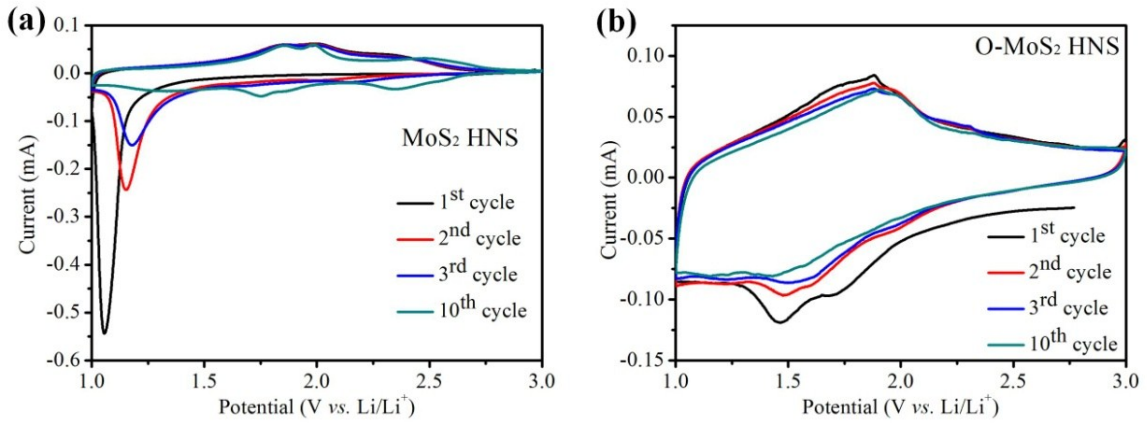

Figure S15. CV curves of (a) MoS_2 HNS and (b) O-MoS_2 HNS at 0.1 mV s^{-1} between 1−3 V. In the H-MoS_2 system, its CVs display a prominent redox peak at 1.1 V vs Li/Li^+, which is associated with the voltage plateau of 2H phase MoS_2. As can be seen, the redox peaks at 1.1 V becomes weak following the cycles and nearly disappear at the 10th cycle. The large differential charge responses are caused by the 2H to 1T phase transition during the cycle process. As for HO-MoS_2, its CV curves show unobvious changes in the subsequent cycles.

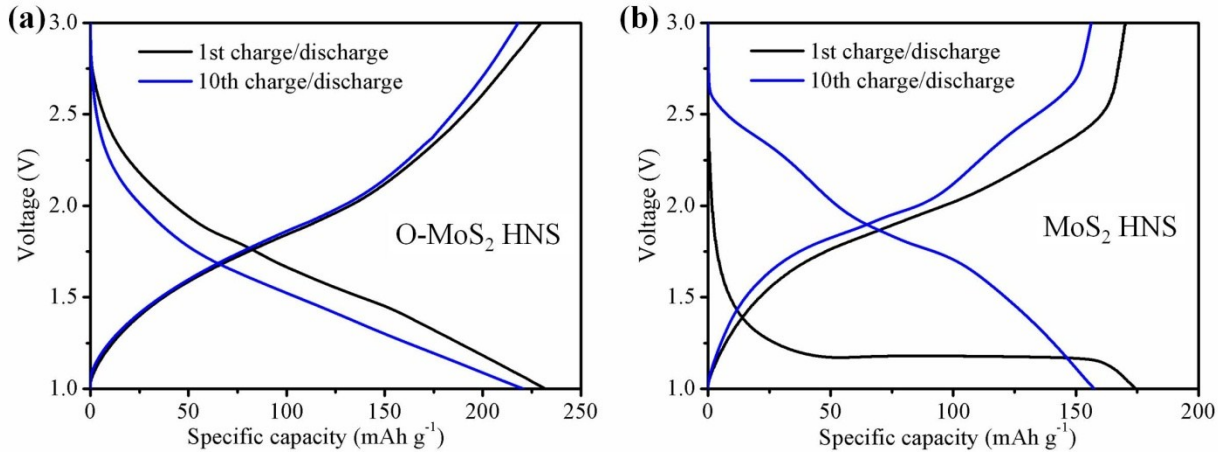

Figure S16. The 1st and 10th galvanostatic charge/discharge curve of (a) O-MoS_2 HNS and (b) MoS_2 HNS. The comparison of the charge/discharge curves at the first and 10th cycle for both samples reveals the two-phase behavior of MoS_2 HNS (obvious voltage plateau at around 1.2 V) during the first cycle. While O-MoS_2 HNS shows the single-phase behavior during Li-ion

intercalation/deintercalation (slope curve).

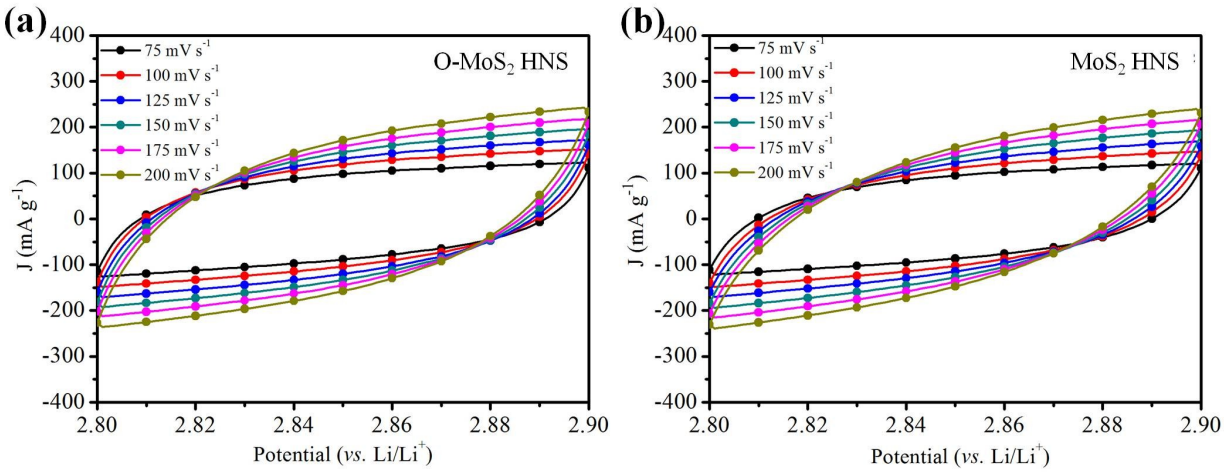

Figure S17. CV curves of (a) O-MoS_2 HNS and (b) MoS_2 HNS at various scan rates at a selected potential range of 2.80−2.90 V *vs* Li/Li^+.

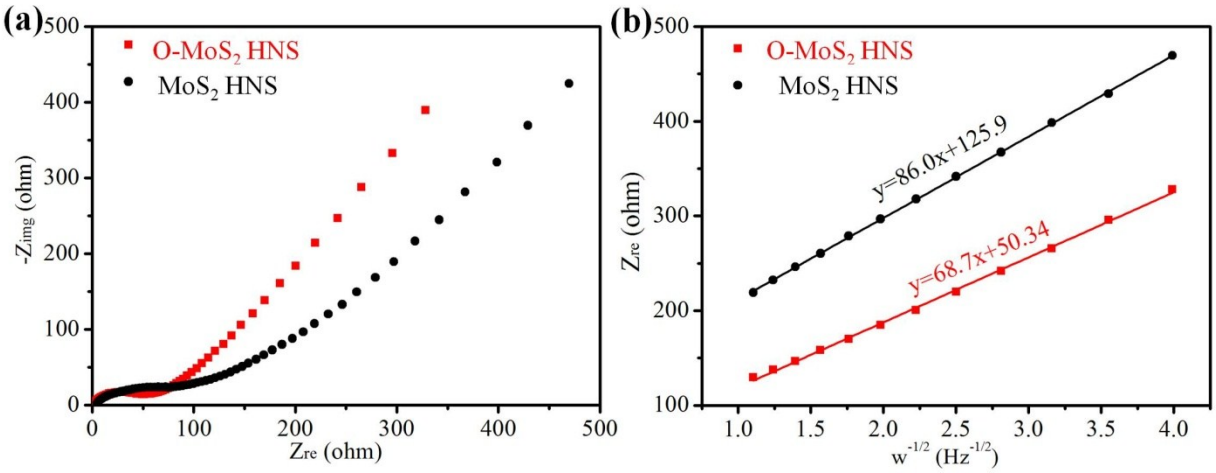

Figure S18. (a) Nyquist plots of O-MoS_2 HNS and MoS_2 HNS electrodes after the 10th cycles. (b) Linear fits of the relationship between Z_{re} and $\omega^{-0.5}$ in the low-frequency region corresponding to (a).

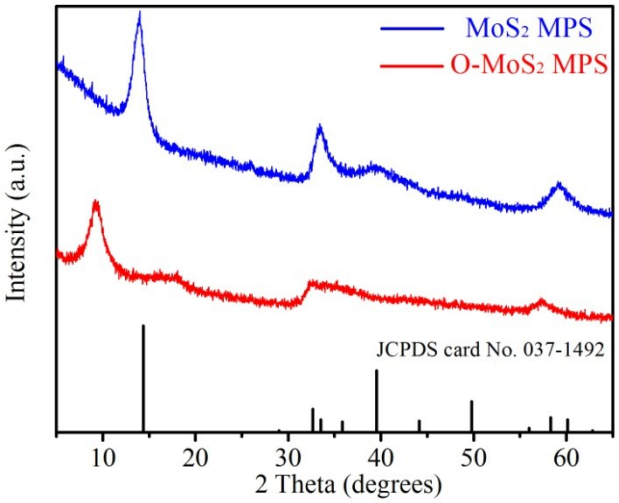

Figure S19. (a) XRD patterns of O-MoS_2 MPS and MoS_2 MPS.

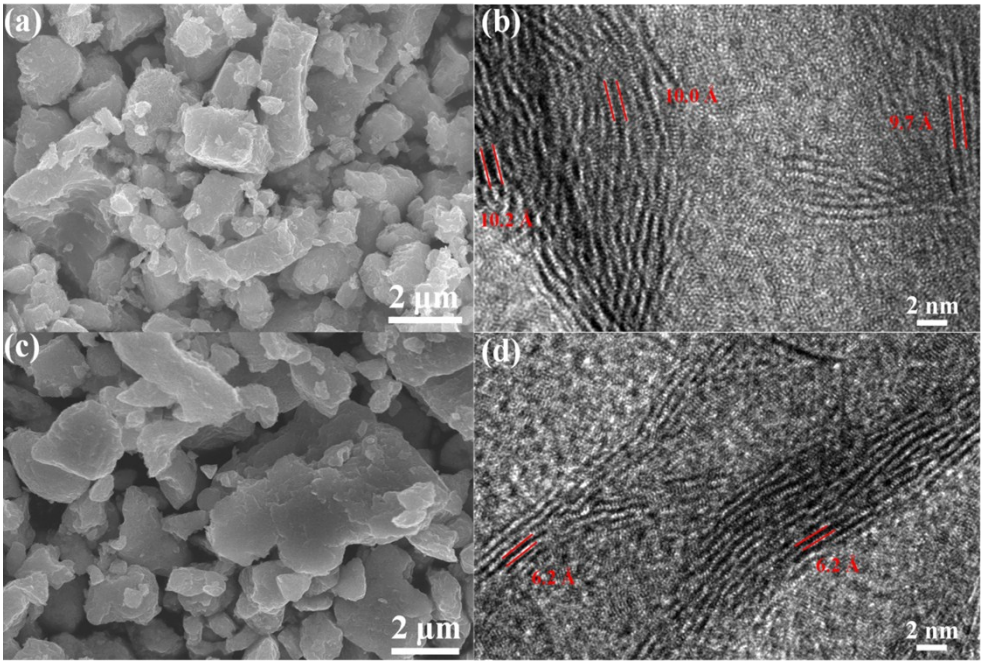

Figure S20. (a) SEM and (c) HRTEM images of O-MoS_2 MPS; (b) SEM and (d) HRTEM images of MoS_2 MPS.

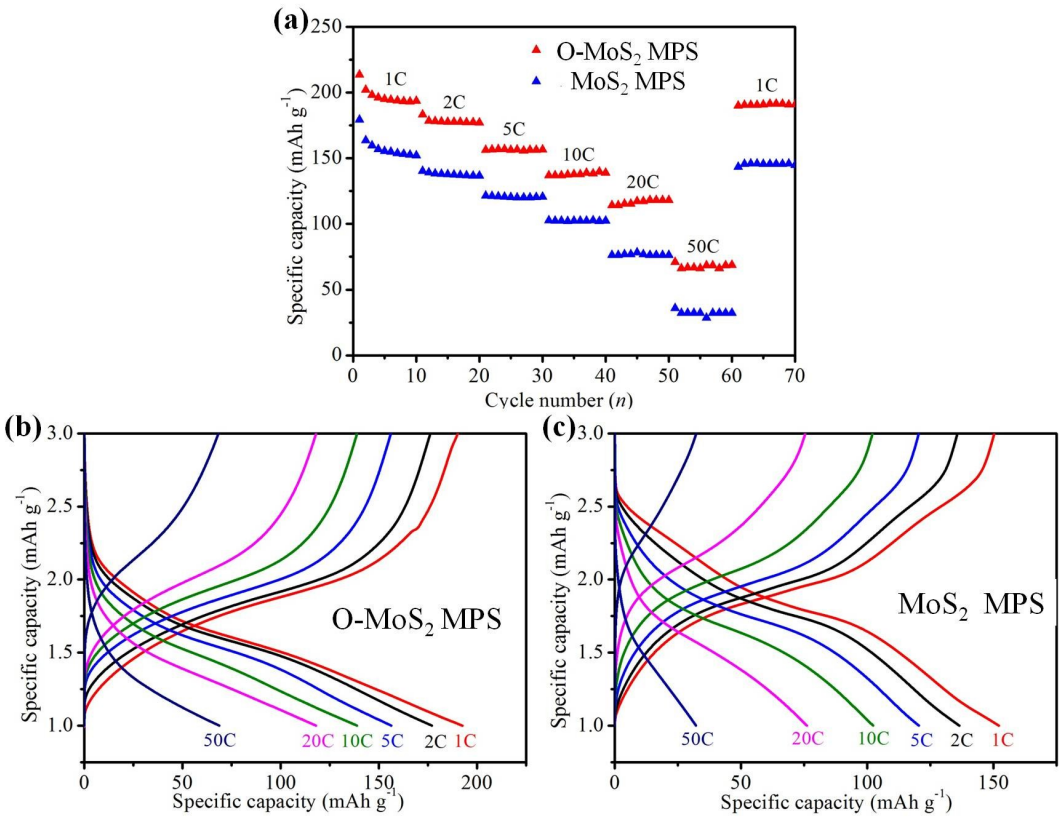

Figure S21. (a) Comparison of the rate performances of O-MoS_2 MPS and MoS_2 MPS at various rate currents. The galvanostatic charge/discharge curves of (b) O-MoS_2 MPS and (c) MoS_2 MPS the curves are based on the 10th cycles of various rate currents in (a).

References:

1 J. Wang, J. Polleux, J. Lim and B. Dunn, *J. Phys. Chem. C.*, 2007, **111**, 14925-14931.

2 H. Lindstrom, S. Sodergren, A. Solbrand, H. Rensmo, J. Hjelm, A. Hagfeldt and S. E. Lindquist, *J. Phys. Chem. B*, 1997, **101**, 7717-7722.

3 T. C. Liu, W. G. Pell, B. E. Conway and S. L. Roberson, *J. Electrochem. Soc.*, 1998, **145**, 1882-1888.

4 B. Chen, E. Liu, T. Cao, F. He, C. Shi, C. He, L. Ma, Q. Li, J. Li and N. Zhao, *Nano Energy*, 2017, **33**, 247-256.